The Astrophysical Journal, 991:229 (13pp), 2025 October 1 https://doi.org/10.3847/1538-4357/adf1e7

The 2021 Hot-type Symbiotic Outburst of YY Herculis: An Optical Follow-up Study

L. S. Sonith[1,2] and U. S. Kamath[1,2]
[1] Indian Institute of Astrophysics, Koramangala, 560034, Bangalore, India
[2] Pondicherry University, R. V. Nagar, Kalapet, 605014, Puducherry, India
Received 2024 November 12; revised 2025 July 11; accepted 2025 July 11; published 2025 September 30

Abstract

We have followed up on the hot-type classical symbiotic outburst reported in YY Her using the Himalayan Chandra Telescope. The outburst coincides with the secondary minima of the system. Approximately 12 similar brightening events have been reported between 1890 and 2020, with only the 1993 outburst being studied spectroscopically. In our study, we monitored the system from 2021 to 2023, covering ∼1.5 orbital cycles, providing an opportunity to understand the spectral evolution of the outburst over a complete orbital period of YY Her. We found that the temperature and luminosity estimations based on emission line fluxes exhibit orbital phase dependence. The values estimated at phase 0.5, corresponding to the secondary minimum, were the most reliable. The temperature of the hot component is $\approx 1.41 \times 10^5$ K, and the luminosity is $\approx 1020\,L_{\odot}$ during the outburst, reduced to $\approx 1.3 \times 10^5$ K and $\approx 830\,L_{\odot}$ after one orbital cycle at phase 0.5. Temperature estimations during the outbursts suggest that YY Her exhibits both hot-type (2021) and cool-type (1993) behavior, similar to another symbiotic star, AG Dra. Using variations of the Ca II absorption lines, we confirmed the contribution of the ellipsoidal effect in secondary minima in the YY Her light curve.

Unified Astronomy Thesaurus concepts: Symbiotic binary stars (1674); Z Andromedae stars (1835); Spectroscopic binary stars (1557); Spectrophotometry (1556); Spectroscopy (1558)

1. Introduction

Symbiotic stars are long-period interacting binaries consisting of a mass-losing giant of a late spectral type and a hot component, typically a white dwarf (WD), surrounded by a circumstellar nebula (see the reviews by J. Mikołajewska 2012 and U. Munari 2019). Symbiotic stars exhibit variability as a result of orbital motion and occasional outbursts. Three different types of outbursts are reported in symbiotic stars: symbiotic novae or slow novae, symbiotic recurrent novae, and classical symbiotic outbursts (Z And-type). Symbiotic novae and symbiotic recurrent novae are rare events, since they require prolonged mass accretion onto the surface of a WD before a thermonuclear runaway can be triggered. In contrast, classical symbiotic outbursts are commonly seen outbursts in symbiotic stars, typically showing 1–3 B mag brightening. These outbursts are either caused by the release of potential energy from extra-accreted matter or by a shift in the emission of the hot component toward longer wavelengths, resulting from a radius expansion followed by an increased mass accretion rate (U. Munari 2019). A detailed study by R. González-Riestra et al. (1999) on the classical symbiotic outbursts of AG Dra using the International Ultraviolet Explorer (IUE) combined with optical observations showed that they can be further classified into hot and cool types based on the temperature of the hot component during the outburst relative to its quiescent temperature. During 2007–09 outbursts of AG Dra, U. Munari et al. (2009) noted that the He II to Hβ ratio is enhanced during the hot-type outburst, while it is reduced during the cool-type outburst.

The photometric variability of YY Her was first identified by M. Wolf (1919), and further observations by L. Plaut (1932) and S. Bohme (1939) contributed to its classification as an irregular variable. Later, G. H. Herbig (1950) classified YY Her as a symbiotic star based on its spectral features such as TiO band heads typical of M2-type giants, along with emission lines of H I, He I, He II, and O [III] and noted its close resemblance with other classical symbiotic stars AX Per, CI Cyg, and Z And. U. Muerset et al. (1991) found that the hot component in the system is a WD with a temperature of 10^5 K and luminosity of $1100\,L_{\odot}$ based on modeling IUE spectra.

A detailed study of the light curves of YY Her from 1890 to 1996 is discussed in U. Munari et al. (1997b), where it was reported to show four outbursts during 1914–19, 1930–33, 1981–82 and 1993–96, along with six small eruptions during 1890, 1903, 1942, 1954, 1965, and 1974. The author also estimated the orbital period of the system, $P = 590$ days, with a visual amplitude of <0.3 mag. A later study by L. Formiggini & E. M. Leibowitz (2006) estimated the orbital period of 593.2 days and found a steady decline of the system from 1890 up to 2001, with a rate of 0.01 mag per 1000 days, suggestive of a past symbiotic nova.

The first detailed spectroscopic study of the YY Her outburst (1993) performed by U. Munari et al. (1997a), in which the temperature of the hot component during the outburst was estimated to be 8.5×10^4 K, dropping from 1.1×10^5 K in quiescence, while the bolometric luminosity of the hot component increased by a factor of ⩾6. Further studies by A. A. Tatarnikova et al. (2000) confirm that the hot component of YY Her is accompanied by increased brightness and reduced temperature during the 1993 outburst. They also suggest that the cool component of YY Her fills its Roche lobe; most of the emission measure of the gaseous envelope is concentrated around the hot component with sharp boundaries, and the system is observed nearly edge-on. Furthermore, high-resolution observations by A. A. Tatarnikova et al. (2001) during the outburst revealed P Cyg profiles in the He I 5876

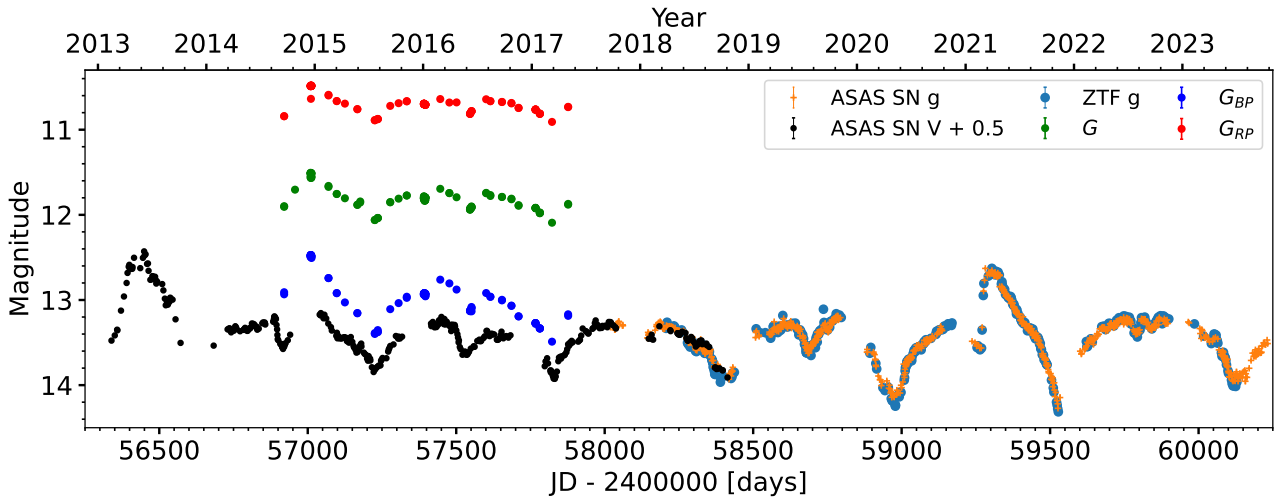

Figure 1. YY Her outburst light curve shown in multiband photometry available from GAIA, ASAS-SN, and ZTF. The 2013 and 2021 outbursts are visible in the light curve. An offset is applied to ASAS-SN *V* band for clarity.

and 7065 Å lines, with moderate outflow velocities ($\sim$100 km s^{-1}).

L. Hric et al. (2001) published long-term CCD photometric data and identified secondary minima in the light curve, which were later confirmed by E. A. Kolotilov et al. (2002). YY Her belongs to a group of symbiotic stars that exhibit secondary minima in their light curves. (e.g., CI Cyg, BF Cyg; J. Mikołajewska et al. 2003). J. Mikołajewska et al. (2002) suggested that secondary minima arise from a combination of ellipsoidal modulation caused by the distorted giant and sinusoidal variation of the nebular continuum. Alternative explanations to secondary minima, such as WD eclipsing with an optically thick envelope surrounding it (L. Hric et al. 2001, 2006) and star spots (L. Formiggini & E. M. Leibowitz 2006), are also proposed to explain this phenomenon.

Since the 1993 outburst, two additional outbursts were reported in 2003–05 and 2013 (U. Munari et al. 2013); however, follow-up studies were sparse. During 2021 February, YY Her underwent a new outburst, reported by K. Sokolovsky et al. (2021) in the Astronomers Telegram. The authors estimated a CV (unfiltered magnitude with *V*-band zero-point) of 11.87 mag on 2021 March 15.006 UTC—much brighter than the average quiescent CV of $\sim$13 mag. Furthermore, they identified that the rise in magnitude began on 2021 February 25.60 UT from the All-Sky Automated Survey for Supernovae (ASAS-SN) *g*-band light curve. Subsequent photometric and spectroscopic observations by U. Munari et al. (2021) revealed a strengthened blue continuum and significantly enhanced emission line fluxes compared to observations taken 583 days earlier, close to the orbital period of YY Her (593.09 days). It was concluded that YY Her is undergoing a hot-type classical symbiotic outburst. Ultraviolet observations from the Swift UVOT instrument by N. Masetti & U. Munari (2021) estimated an unabsorbed UV luminosity of 730 $L_{\odot}$ assuming 8.2 kpc distance and interstellar reddening $E(B-V) = 0.2$ mag. The source remained undetected in X-ray observations taken using the Swift X-ray Telescope with an unabsorbed flux upper limit $<3 \times 10^{-13}$ erg cm^{-2} s^{-1}.

We followed up on the hot-type classical symbiotic outburst reported in YY Her using the Himalayan Chandra telescope (HCT) from 2021 to 2023. Long-term follow-up observations covering the outburst and one additional orbital cycle allowed us to understand the evolution of different parameters during the outburst and identify the effect of the orbital phase on their estimation.

In Section 2, we describe the observational data used in our study. The light-curve analysis and orbital period estimation are discussed in Section 3.1. Distance and reddening values are determined in Section 3.2. The spectral energy distribution (SED) is discussed in Section 3.3. In Section 3.4, spectral and line evolution are discussed. The temperature and luminosity estimation of the hot component is described in Section 3.5. The discussions and important results are summarized in Sections 4 and 5, respectively.

2. Observations

2.1. Photometry

2.1.1. ASAS-SN, ZTF, and GAIA

We obtained *V*- and *g*-band light curves for YY Her from the ASAS-SN (B. J. Shappee et al. 2014; C. S. Kochanek et al. 2017), spanning JD 2456371.07 to JD 2460232.63 (2013 March 19–2023 October 15), and *g*-band photometry from the Zwicky Transient Facility (ZTF; F. J. Masci et al. 2019; ZTF Team 2025) spanning JD 2458204.0 to JD 2460128.93 (2018 March 26–2023 July 3). Additionally, we obtained *G*, G_{BP}, and G_{RP} band magnitudes from Gaia DR3 (Gaia Collaboration et al. 2016, 2023) covering the period JD 2456920.49 to JD 2457876.99 (2014 September 19 to 2017 May 3). Figure 1 displays the Gaia, ASAS-SN, and ZTF light curves. The higher cadence *g*-band data from ZTF and ASAS-SN overlapped in time.

2.1.2. GIT

We carried out photometric observations from the GROWTH-India Telescope[3] (GIT; H. Kumar et al. 2022a), a fully robotic 0.7 m telescope located at the Indian Astronomical Observatory (IAO), Hanle, India. Observations are taken in Sloan Digital Sky Survey (SDSS) *griz* prime filters, from JD 2459618.5 to JD 2460116.3 (2022 February 8–2023 June 20),

[3] https://sites.google.com/view/growthindia/about

covering the subsequent orbital cycle of YY Her from primary minima after the 2021 outburst. The telescope is equipped with a 4096 × 4108 Andor iKon-XL CCD, with an image scale of 0.″67 per pixel and a field of view of 0.°7. The GIT images were preprocessed by an automated pipeline, which performs bias subtraction, flat-field correction, and cosmic-ray removal (H. Kumar et al. 2022b). Magnitudes are estimated using point-spread function photometry, and zero-points of individual filters are estimated using Pan-STARRS field observations. The *griz*-band photometric data are tabulated in Table A1 in the Appendix.

2.1.3. AAVSO

We obtained publicly available photometry from the American Association of Variable Star Observers (AAVSO;[4] B. K. Kloppenborg 2023) International Database. The data consist of CCD and CMOS photometry across various filters, as well as visual estimates. We used *V*-band photometric data spanning JD 2451760.7 to 2460169.3 (2000 August 4–2023 August 12) to construct a long-term light curve for period estimation in our study.

2.1.4. Photometry from Literature

Since the 1993 outburst of YY Her, multiple studies have investigated its photometric behavior and published follow-up photometric data (U. Munari et al. 1997b; A. A. Tatarnikova et al. 2000, 2001; L. Hric et al. 2001, 2006; E. A. Kolotilov et al. 2002; J. Mikołajewska et al. 2002). We compiled CCD and photoelectric-based *V*-band data from these works to construct a long-term light curve. Data from L. Hric et al. (2006) were corrected to account for zero-points associated with different observation facilities, as specified in the original paper.

2.2. Spectroscopy

Spectroscopic follow-up observations of YY Her outburst were carried out between 2021 March 18 and 2023 August 7. Low-resolution optical spectra were obtained from the Himalayan Faint Object Spectrograph Camera (HFOSC) mounted on the 2 m HCT. Spectra cover the wavelength range of 3800 Å–7500 Å in the grism 7 (Gr7) configuration and 5400 Å–9000 Å in the grism 8 (Gr8) configuration with a resolution of $R \sim 1300$ and 2200, respectively. Data reduction was carried out following standard procedures such as bias subtraction, flat-fielding, and extraction tasks in the Image Reduction and Analysis Facility (IRAF[5]). We achieve this using the pipeline based on PyRAF modules, which uses the IRAF tasks inside. After wavelength calibration and response correction using standard stars, grism 7 and grism 8 spectra were combined to get the final spectra. The combined spectra were converted to an absolute flux scale by matching the synthetic photometry (calculated using the SDSS *g* prime filter transmission profile from the SVO Filter Profile Service, C. Rodrigo et al. 2012) to the ASAS-SN *g*-band photometry. The calibration adopted the AB magnitude system, with a zero-point flux density of 3631 Jy. The propagation of errors is carried out in all steps, including the extraction to the absolute flux calibration, and is explained in detail in L. S. Sonith & U. S. Kamath (2023). The log of observations is given in Table 1.

Table 1
Observational log for Spectroscopic Data Obtained for YY Her

Date (yyyy-mm-dd)	JD	Exposure Time (s)	Wavelength Range (Å)
2021-03-18	2459292.48	180 + 180	3600–9000
2021-03-20	2459294.48	120 + 120	3600–9000
2021-03-22	2459296.44	180 + 180	3600–9000
2021-03-24	2459298.41	120 + 120	3600–9000
2021-03-26	2459300.42	120 + 120	3600–9000
2021-04-03	2459308.48	120 + 120	3600–9000
2021-04-07	2459312.34	120 + 120	3600–9000
2021-04-25	2459330.40	120 + 120	3600–9000
2021-05-01	2459336.41	180 + 180	3600–9000
2021-07-17	2459413.34	180 + 180	3600–9000
2021-08-17	2459444.22	360 + 360	3600–9000
2021-08-24	2459451.24	180 + 180	3600–9000
2021-09-01	2459459.26	180 + 180	3600–9000
2021-10-13	2459501.08	180 + 180	3600–9000
2021-10-22	2459510.11	180 + 180	3600–9000
2022-02-11	2459621.52	180 + 180	3600–9000
2022-03-08	2459647.44	300 + 300	3600–9000
2022-03-21	2459660.45	300 + 300	3600–9000
2022-05-09	2459709.38	180 + 180	3600–9000
2022-06-11	2459742.30	180 + 180	3600–9000
2022-08-30	2459822.28	240 + 240	3600–9000
2022-10-01	2459854.13	240 + 60	3600–9000
2023-03-02	2460006.39	900 + 900	3600–9000
2023-06-10	2460106.31	180 + 180	3600–9000
2023-08-07	2460164.17	180 + 180	3600–9000

3. Results

3.1. Optical Light Curve of YY Her

3.1.1. Periodic Behavior

The optical light curve of YY Her from 2013 to late 2023, consisting of data from Gaia, ASAS-SN, and ZTF, is shown in Figure 1. A 0.5 mag offset is applied to the ASAS-SN *V* band. Primary and secondary minima are visible in the light curve. We estimated the periodicity of the light curve using Lomb–Scargle periodogram (LSP; N. R. Lomb 1976; J. D. Scargle 1982) and obtained periods of 579.19 and 578.92 days corresponding to the highest peaks in the ASAS-SN *g* and ZTF *g* bands, and a period of 525.77 days in a closer peak in the ASAS-SN *V* band. Similarly, we obtained periods of 604.71 days for the AAVSO *V* band and 583.61 days corresponding to the nearest peak for previously published *V*-band measurements (hereafter Literature *V*; see Section 2.1.4).

To improve period estimation, we constructed a long-term light curve combining photometric data from ASAS-SN *g*, ZTF *g*, ASAS-SN *V*, AAVSO *V*, and Literature *V* measurements (see Figure 2). A 0.5 mag shift was applied to all *V*-band data to align it with the *g* band. The LSP analysis of the combined data set shows a major peak at 594.08 days, corresponding to the primary minima, and a secondary peak at 282.95 days, associated with the secondary minima. Both peaks have a false alarm probability of <0.01%. The resulting periodograms are presented in Figure 3.

[4] https://www.aavso.org

[5] IRAF is distributed by the National Optical Astronomy Observatory, which is operated by the Association of Universities for Research in Astronomy (AURA) under a cooperative agreement with the National Science Foundation.

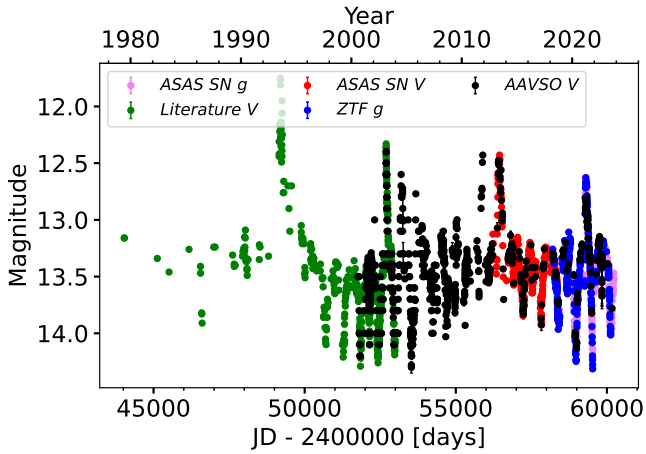

Figure 2. Combined *V*- and *g*-band data from ASAS-SN, ZTF, AAVSO, and literature after applying the appropriate shift (see text for details).

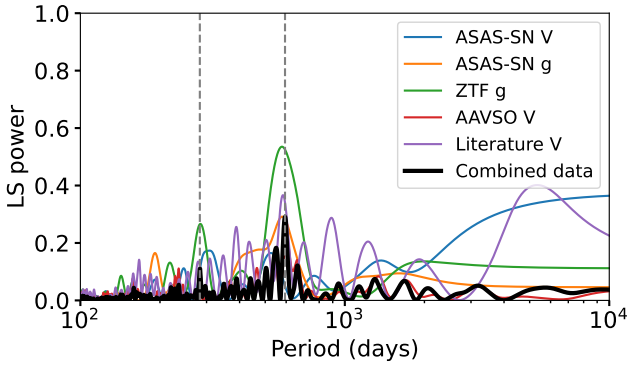

Figure 3. LSP of YY Her using ASAS-SN *g* and *V* band, ZTF *g*-band, AAVSO *V*-band, *V* data compiled from the literature, and combined data is plotted (see text for details). The period corresponding to primary minima and secondary minima is marked with dashed lines.

Using the period of primary minima obtained from LSP, we initially fitted a single sinusoidal model and derived a period of 594.27 ± 0.5 days. We also attempted to fit a combination of two sinusoidal curves (hereafter double-sinusoidal model) representing periods of primary minima and secondary minima (see Figure A1). The double-sinusoidal model provides a lower chi-square fit compared to a single sinusoidal model and we estimated a period of 593.09 ± 0.30 days, which is in agreement with the previous estimate of L. Formiggini & E. M. Leibowitz (2006) within the margin of error and closer to the period estimation based on the long-term light-curve study by U. Munari et al. (1997b). Hence, we adopted the ephemeris based on a double-sinusoidal fit given by Equation (1) to calculate the orbital phase for the rest of the paper

$$\mathrm{JD_{min}} = 2458968.13 \pm 2.04 + 593.09 \pm 0.30 \times E. \quad (1)$$

Phase (ϕ) = 0.0 corresponds to the inferior conjunction of the cool giant, coinciding with the primary minima, while $\phi = 0.5$ corresponds to the superior conjunction. Hereafter, when the phase is written within the range $0 \leqslant \phi \leqslant 1$, it corresponds to a repeating phase interval unless specified with an exact date (e.g., 0.5 represents 0.5, 1.5, 2.5, etc.)

Gaia $G_{\rm BP}$, G, and $G_{\rm RP}$ light curve indicates that during the minimum, the largest amplitude is observed in the $G_{\rm BP}$ band (blue), while it is weaker in the $G_{\rm RP}$ band (red). This

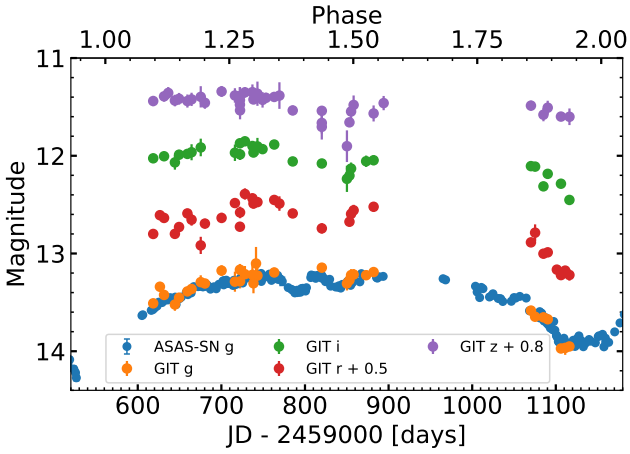

Figure 4. YY Her light curve shown in the GIT multiband photometry. Phase estimated based on the ephemeris given in Equation (1). Offsets are applied for clarity.

trend aligns with observations in other shell-burning symbiotic stars, where irradiation from burning WD significantly influences the blue spectral region (e.g., TCP J18224935-2408280; L. S. Sonith & U. S. Kamath 2023). The modulation can be explained by a combination of the reflection effect (T. S. Belyakina 1970; S. J. Kenyon 1986) and orbital variation in nebular contribution (A. Skopal 2001; J. Mikołajewska et al. 2002).

In Figure 1, we observe secondary minima in the light curve throughout all orbital cycles from 2014. In addition, we note that the secondary minima appear slightly shifted toward $\phi \sim 0.45$ (see Figure 4). The secondary minima seen in YY Her are explained by the ellipsoidal effect of the cool giant (J. Mikołajewska et al. 2002). Other alternative explanations include eclipsing by the hotter component surrounded by an optically thick envelope that mimics a main-sequence star in terms of radius (L. Hric et al. 2006). We favor the interpretation of the ellipsoidal effect as the primary cause of the observed phenomena. The double-sinusoidal model we used to fit the combined light curve is similar to the phenomenological model proposed by J. Mikołajewska et al. (2002). However, we noticed that the secondary minima are steeper than in our model. We further explore the cause of secondary minima in Section 3.4.1, where we analyze the variation of the Ca II line during the orbital cycle.

3.1.2. Outburst Light Curve

YY Her underwent two outburst events in the last 10 years —2013 and 2021 (U. Munari et al. 2013; K. Sokolovsky et al. 2021). ASAS-SN and ZTF *g* band show that the YY Her 2021 outburst began around 2021 February 25 and peaked at 12.62 mag with an approximately 1 mag brightening event. The outburst coincided with secondary minima, which hindered an accurate estimation of the amplitude of the outburst. The 2013 outburst in the *V*-band light curve also shows a brightening of ~1 mag. Compared to the 1994–96 outburst reported in YY Her (U. Munari et al. 1997a), the 2021 outburst had a lower amplitude. Hot-type outbursts typically show a lower optical brightening than cool-type classical symbiotic outbursts. This is also seen in previously reported AG Dra outbursts (R. González-Riestra et al. 1999).

Interestingly, the primary minima observed before and after the 2021 outburst showed a more significant reduction in brightness (dimmer by ∼0.2 mag) compared to other primary minima in the light curve. Similar behavior was observed by U. Munari et al. (1997b) during previous outbursts. This enhanced depth of minima may stem from increased stellar wind activity originating from the giant star during this period.

From the ASAS-SN and ZTF g-band light curves, we observed a notable reduction in the secondary minima in the subsequent orbital cycle following the outburst. In fact, it looked like a smaller peak inside a secondary minima (see Figures 1 and 4). The GIT light curve obtained during the same period suggests that the increase in magnitude during secondary minima is only significant in the g band, not in the r, i, z bands (see Figure 4). After the 2021 outburst, the hot component (WD) remains significantly heated, causing an increase in magnitude in the blue band (g) during $\phi \sim 1.45$, when the hot component is visible to the observer. This should be taken with caution, as we have hardly any photometric points during secondary minima in GIT photometry. A similar brightening in the g-band light curve following the classical symbiotic outburst in TCP J18224935-240828 is reported by L. S. Sonith & U. S. Kamath (2023); however, for YY Her, it is limited to the secondary minima, possibly due to the high inclination.

3.2. Distance and Reddening

In our study, we used Gaia EDR3 parallaxes to determine the geometric and photogeometric distances to YY Her, using the method by C. A. L. Bailer-Jones et al. (2021). The geometric distance was calculated as $6.9^{+1.3}_{-1.2}$ kpc, while the photogeometric distance was found to be $5.4^{+0.8}_{-0.6}$ kpc. Our SED fitting, discussed in Section 3.3, provided a distance estimate of $5.2^{+0.4}_{-0.3}$ kpc, close to the photogeometric distance. The goodness of fit of the astrometric model is −1.5 for Gaia EDR3. A lower than 3 is considered a good fit.[6] Gaia distance estimation is based on a Bayesian probabilistic approach, which uses a prior constructed from a 3D model of our Galaxy, assuming that all sources are single stars. This may introduce significant uncertainties when estimating distances for binary systems. We have adopted the photogeometric distance given by C. A. L. Bailer-Jones et al. (2021) in this paper.

Reddening map by E. F. Schlafly & D. P. Finkbeiner (2011) gives a visual extinction value, $A_v = 0.26^{+0.2}_{-0.2}$ in the direction of YY Her. In addition, we also determined visual extinction $A_v = 0.29^{+0.1}_{-0.1}$ in the direction of YY Her for the estimated Gaia photogeometric distance, using the 3D map of interstellar dust reddening by G. M. Green et al. (2019). The value of A_v did not show significant differences beyond 1.3 kpc. The error associated with A_v is determined from the posterior distribution. In our paper, we adopt the value $A_v = 0.29^{+0.1}_{-0.1}$. Reddening corrections are applied using the extinction law proposed by E. L. Fitzpatrick (1999).

3.3. Spectral Energy Distribution of Cool Component in YY Her

G. H. Herbig (1950) initially assigned a spectral type of M2 to the cool giant in YY Her. Subsequent studies by S. J. Kenyon & T. Fernandez-Castro (1987) classified the secondary as an M3-type cool giant, while U. Munari et al. (1997a) estimated it to be of M4 type.

We determined the spectral type by constructing an SED using photometric data from Gaia DR3 (G_{RP}; Gaia Collaboration et al. 2016, 2023), APASS (r', i'; A. Henden & U. Munari 2014), Two Micron All Sky Survey (J, H, K_s; M. F. Skrutskie et al. 2006), and Wide-field Infrared Survey Explorer (W1, W2; E. L. Wright et al. 2010) (see Figure 5). The cool component in the symbiotic star dominates in redder wavelengths, whereas the contribution from the nebula and WD is higher in the bluer wavelengths. Hence, we only considered filters above 6000 Å in our SED. The SED modeling is performed using the ARIADNE[7] (J. I. Vines & J. S. Jenkins 2022), which uses synthetic model atmospheres, including PHOENIX v2 (T. O. Husser et al. 2013), BT-NextGen (P. H. Hauschildt et al. 1999; F. Allard et al. 2012), BT-Settl (F. Allard et al. 2012), and BT-Cond

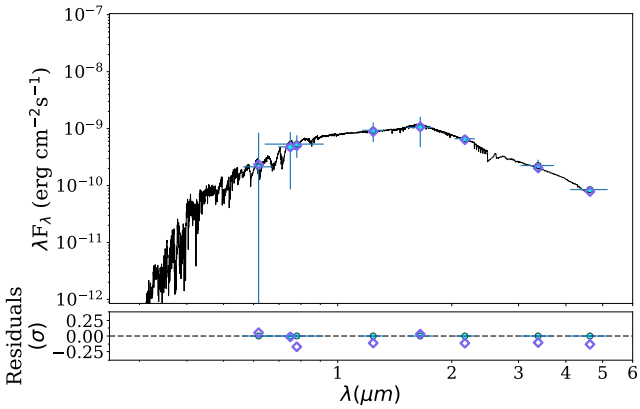

Figure 5. Spectral energy distribution of the YY Her obtained from different photometric bands (see Section 3.3 for details).

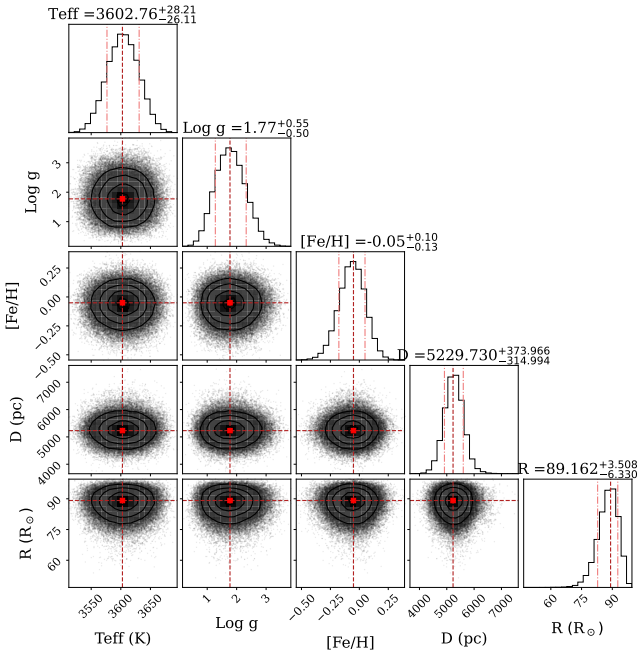

Figure 6. Corner plot showing various parameters derived from SED fitting using synthetic model atmospheres.

[6] https://gea.esac.esa.int/archive/documentation/GDR2/Gaia_archive/chap_datamodel/sec_dm_main_tables/ssec_dm_gaia_source.html

[7] https://github.com/jvines/astroARIADNE

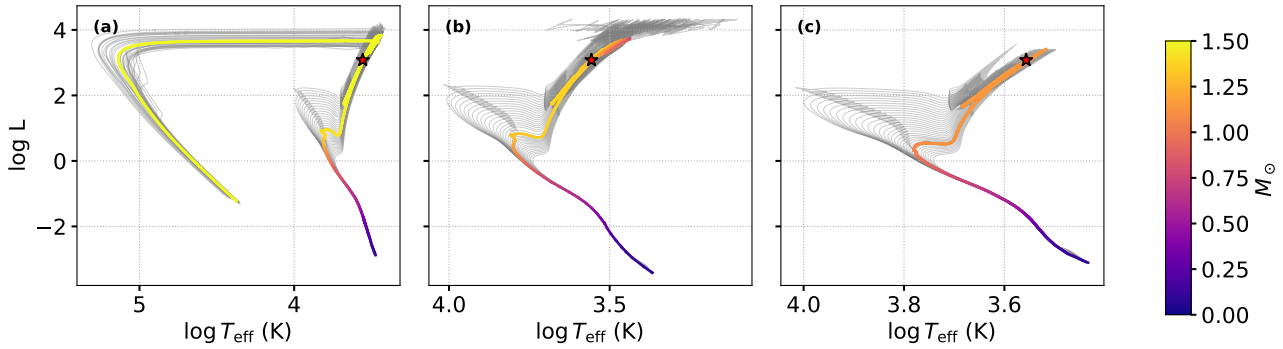

Figure 7. H-R diagrams showing stellar isochrones from (a) MIST, (b) PARSEC, and (c) BaSTI models. The red star with error bars marks the observed effective temperature and luminosity of the cool giant derived from the SED fit.

(F. Allard et al. 2012), employing Bayesian model averaging techniques to optimally constrain parameters.

We used the temperature prior based on the Gaia temperature estimate and its upper limit. The distance prior is taken from a geometric distance estimate from Gaia (see Section 3.2), with the highest error serving as the upper limit. The A_v value is fixed at 0.29. Additionally, we employ a uniform prior for log g ranging from 0 to 4, derived from our initial fitting, resulting in a radius estimation within the giant star regime. Default priors are used for radius and metallicity. The best fit yields a temperature of $3602.76^{+28.21}_{-26.11}$ K, log $g = 1.77^{+0.55}_{-0.50}$, radius $= 89.16^{+3.51}_{-6.33}$ $R_\odot$ and luminosity $= 1248^{+287.6}_{-215.7}$ $L_\odot$. These results correspond to a cool giant of M2 spectral type. The corresponding SED parameters are shown in Figure 6. The mass of the cool giant is estimated by interpolating the best-fit temperature and luminosity from the SED analysis within stellar isochrones (see Figure 7). The resulting masses are 1.50 $M_\odot$ from MIST (A. Dotter 2016), 1.29 $M_\odot$ from PARSEC (A. Bressan et al. 2012), and 1.14 $M_\odot$ from BaSTI (S. L. Hidalgo et al. 2018).

Considering the phase-dependent variability observed in the YY Her spectra during different observations (see Section 3.4), the SED obtained only explains the global mean of the photometric observations taken. Since we are not modeling and removing the nebular contribution to the SED, the spectral type we have obtained serves as the upper limit. In addition, the spectral type is likely overestimated because the hot WD irradiates the surface of the cool giant. Furthermore, it should be noted that the SED can more accurately constrain parameters such as temperature, radius, and log g, while [Fe/H] serves as a qualitative measure.

3.4. Evolution of Optical Spectra

Spectroscopic monitoring of YY Her covered the declining phase of the 2021 outburst and one subsequent orbital cycle. The outburst coincides with the secondary minima in the light curve, and observations were taken from $\phi = 0.55$ (2021 March 18) to $\phi = 2.02$ (2023 August 7). The follow-up spectroscopic observations are plotted in Figure 8; a few additional spectra taken at closely spaced epochs—providing no new phase coverage—are included in Figure A2. The optical spectra of YY Her show Balmer series lines, He I, O I, high-excitation lines such as He II, and TiO band heads from the cool component throughout the evolution, including outburst, quiescence, and both primary and secondary minima. We also noted that the Raman-scattered O VI band is absent in the spectrum, and O[III], Bowen 4640 lines are present only in particular phases.

Optical spectra during different orbital phases show significant changes in spectral profile (see Figure 8). We further studied this by comparing it with reference spectra of the different spectral types obtained from the MILES library (J. Falcón-Barroso et al. 2011). We found that the spectrum obtained at $\phi =$ 1.49 (2022 October 1) was closely similar to the M2 III, while at $\phi =$ 1.25 and 1.75 (2022 May 9 and 2023 March 2) resembled M3 III (see Figure 9). At $\phi =$ 1.1 (2022 February 11) the spectrum is closely aligned to M4 III. The surface of the cool giant facing the WD has a higher temperature, which is reflected in the estimated spectral types in different phases. During the inferior conjunction of the cool giant, the heated region is least visible and shows a later spectral type (M4 III), while during the superior conjunction, it shows an earlier spectral type (M2 III).

We measured fluxes of all important lines; the dereddened values are listed in Table A2. The flux evolution of the Balmer and He emission lines, and Ca II absorption lines is shown in Figure 10. In the first spectrum, we obtained during the outburst on $\phi = 0.55$ (2021 March 18), emission lines of He II, He I, and O I are significantly strengthened compared to the observation taken on 2022 October 1 at similar $\phi = 1.49$, following one orbital cycle. The Bowen 4640 Å and [O III] 5007 Å lines are also strengthened (see Figure 11). The outburst resulted in an enhanced blue continuum and a significantly strengthened Balmer jump, indicating a rise in the temperature of the ionizing source. We observed an increase in the He II/Hβ ratio during the outburst ($\phi = 0.55$) compared to the similar phase ($\phi = 1.49$) after one orbital cycle. U. Munari et al. (2021) reported similar observations comparing outburst and pre-outburst spectra taken almost 583 days earlier. An increase in the He II/Hβ ratio indicates that the outburst is of hot type.

Spectroscopic follow-up observations show the sinusoidal variability of the Balmer lines (Figure 10), which peak around $\phi = 0.5$. He I 6678 Å and He II 4686 also show a similar trend, but the amplitude variation is lower than the Balmer lines. He I 7280 Å disappears completely near primary minima, a pattern also evident in O I line 8444 Å. A prior study by U. Munari (1989) on multiple S-type symbiotic stars using phase-resolved IUE spectroscopy found that UV emission lines strengthened significantly near $\phi = 0.5$. D. Proga et al. (1996, 1998) explained this phase-dependent variation in emission line strengths using non-LTE illumination models of the red-giant wind.

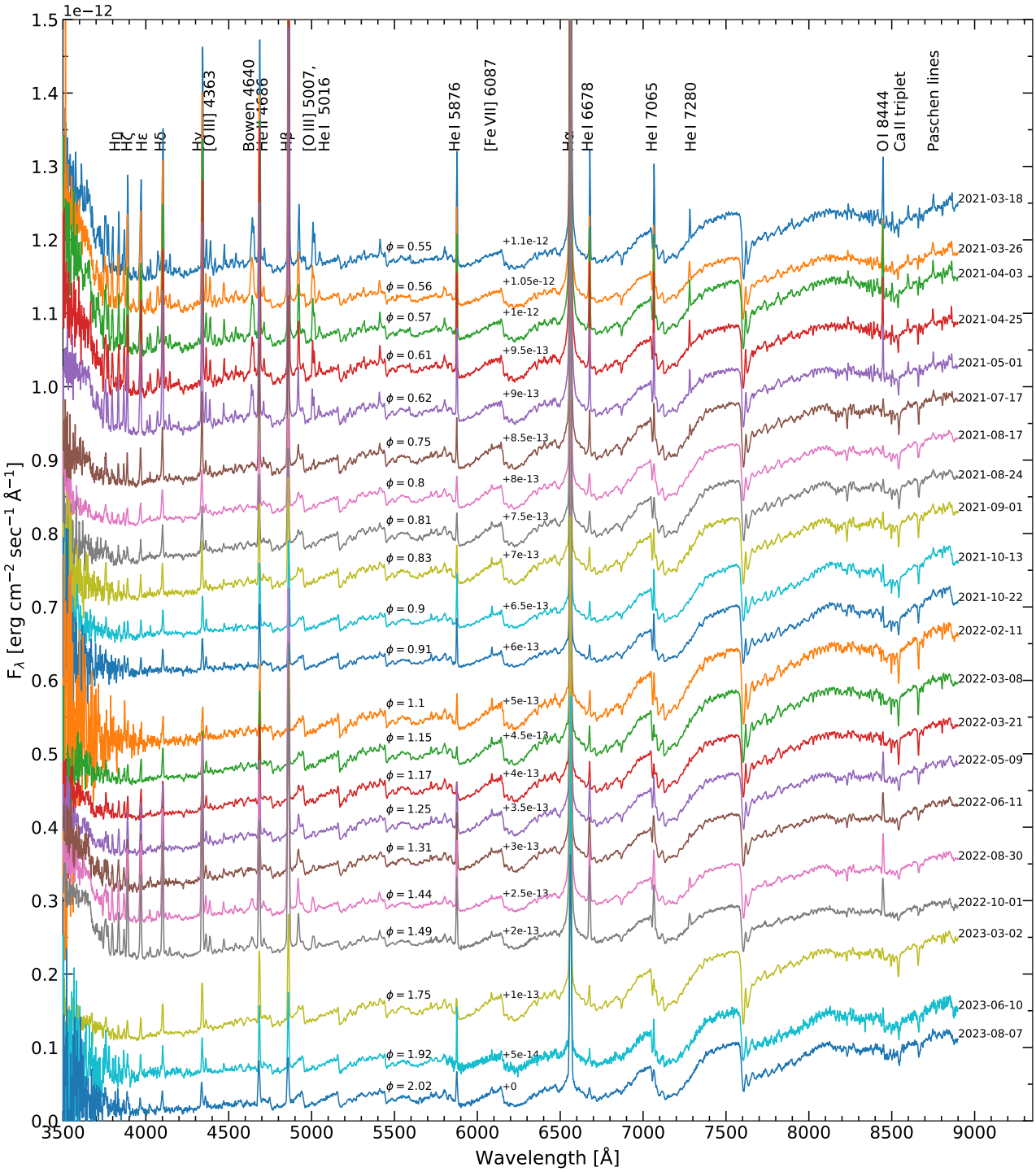

Figure 8. Optical low-resolution spectral evolution of YY Her obtained from 2021 to 2023, covering the outburst and subsequent orbital cycle of YY Her. The identified lines are labeled at the top. Observation date and orbital phase (ϕ) are given for each spectrum. Spectra are shifted to the indicated amount for better visibility. Few observed spectra taken in closer epochs are omitted from this figure; they are plotted in the Appendix (see Figure A2).

The TiO bands appear weaker around $\phi = 0.5$ and strengthen as they approach $\phi = 0$. We estimated the equivalent widths of TiO bands at 7054 and 6159 Å after removing the emission lines and plotted them against the phase (see Figure 12). TiO bands show a periodic variation that arises from the inverse relationship between the temperature and band strength, which is consistent with the spectral types observed at different phases.

The O [III] 5007 Å is clearly identifiable during secondary minima ($\phi = 0.5$) (see Figure 11). The O [III] line was blended with a nearby He I 5016 Å line, and during quiescence ($\phi = 1.49$), the line strength was reduced. Although it remains difficult to observe, the strength of the O [III] line is progressively reduced while moving away from the secondary minima. Notably, the Bowen 4640 Å line is visible only in a very narrow phase interval ($\phi = 0.5 \pm 0.1$) close to the

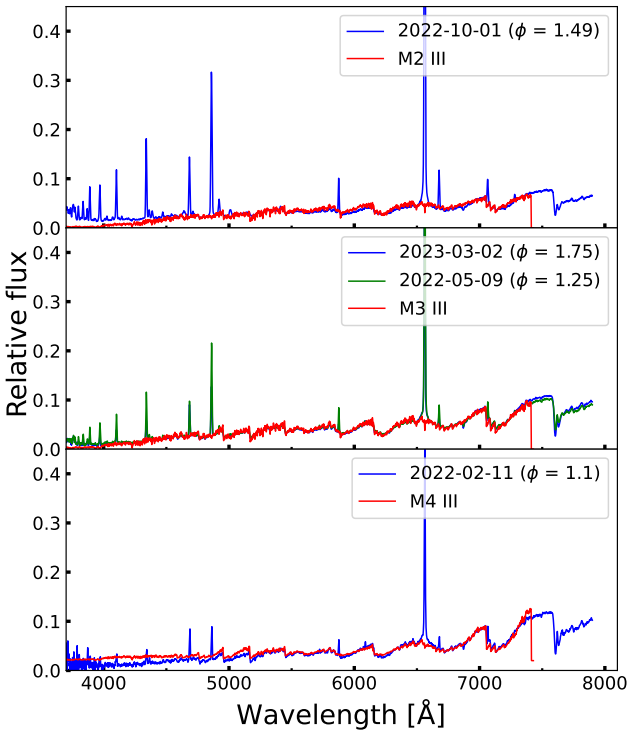

Figure 9. Spectral type comparison plot with phase 0, 0.25/0.75, and 0.5 with respect to M2 III, M3 III, and M4 III spectral types from the MILES library. Spectra are scaled for comparison.

secondary minima. We identified the [Fe VII] 6083 Å line in all phases except during the outburst. This behavior is consistent with observations from outbursts in other symbiotic stars (e.g., TCP J18224935-2408280—L. S. Sonith & U. S. Kamath 2023; AX Per—A. Skopal et al. 2011; FN Sgr—E. Brandi et al. 2005).

3.4.1. Ca II Line Variation

Ca II triplet absorption lines originate from the photosphere of the cool giant in YY Her. We estimated the flux of relatively stronger and less contaminated Ca II 8542 Å, Ca II 8662 Å lines. Ca II lines show variability with half of the orbital period of the system, whereas the Balmer lines and the He lines follow the orbital periodicity (see Figure 10). The origin of such a period is due to the ellipsoidal modulation of the giant star. In Figure 10, we can see that the Ca II lines are strengthened near $\phi =$ 0.25 and 0.75, while they weakened closer to $\phi =$ 0.0 and 0.5.

3.5. Temperature and Luminosity of the Hot Component

The temperature of the hot component in the symbiotic star is estimated using an analytical relation derived by T. Iijima (1981). This method relies on a case B recombination scenario, where the hot source ionizes the surrounding nebula. The relation considers the fluxes of Hβ, He I, and He II lines to determine the temperature, as shown in Equation (2). The temperature estimates are valid between 70,000 and 200,000 K

$$T_{\rm hot}(\text{in } 10^4 \text{ K}) = 19.38 \sqrt{\frac{2.22 F_{\rm He\ II\ 4686}}{4.16 F_{\rm H\beta} + 9.94 F_{\rm He\ I\ 4471}}} + 5.13. \quad (2)$$

The luminosity of the hot component is determined by applying Equation (8) of S. J. Kenyon et al. (1991) and Equation (6) of J. Mikolajewska et al. (1997). These calculations gave consistent results, with both estimates agreeing within 25%. The average of these estimates is provided in Table 2. In addition, we estimated the radius by assuming a blackbody model for the hot component.

The estimated temperatures are given in Table 2 and shown in Figure 10. Interestingly, temperatures calculated from emission line ratios show periodic behavior. This is entirely due to the geometrical effect caused by orbital motion. Due to the high angle of inclination of YY Her, the nebula surrounding the hot component is eclipsed by the giant star to varying degrees in different phases. The change in visibility of the nebular region leads to variations in line ratios, affecting the temperature estimation. It should be noted that the neutral lines (e.g., Balmer lines) originate in a more extended region around the hot component compared to the high ionization lines (e.g., He II 4686 Å), and show a higher degree of variation. Similar effects are observed in luminosity estimation, which is significantly influenced by the Hβ line flux.

Temperatures closer to $\phi = 0.0$ are overestimated, even exceeding values during the outburst ($\geqslant 1.4 \times 10^5$ K). Similar phase dependence of the estimated parameters has been reported by J. L. Sokoloski et al. (2006) in Z And. We tried to address phase variation in temperature and luminosity calculations by introducing correction factors through fitting a sinusoidal function. However, we were unable to achieve a satisfactory fit. A periodic function to correct for the variation may not be sufficient, as this will not account for geometric effects that vary differently across different spectral lines.

The temperature and luminosity estimates obtained during the secondary eclipse are considered more reliable since the WD and the nebular region are directly exposed to the observer. Hence, we only considered the parameter estimated during secondary minima. During the outburst at ($\phi = 0.55$), we estimated $T = \sim$1.41 x 10^5 K, $L = \sim$1020 $L_\odot$, and $R = 0.054$ $R_\odot$. The values after one orbital cycle at ($\phi = 1.49$) are estimated as $T = \sim$1.30 x 10^5 K, $L = \sim$830 $L_\odot$, and $R = 0.056$ $R_\odot$.

4. Outburst Behavior

The classical symbiotic star YY Her showed multiple outburst events in the past. A detailed follow-up study of the 1994–1996 outburst by U. Munari et al. (1997a) and A. A. Tatarnikova et al. (2000) showed that the temperature of the hot component drops during the optical maxima. This indicates that the 1993 outburst was cool-type in nature. Based on line fluxes reported in Table 2 of A. A. Tatarnikova et al. (2000), He II 4876 Å/Hβ ratio during outburst (1993 August 25) was significantly lower than observation taken in a similar phase ($\phi \sim 0.43$) two orbital cycles prior (1990 May 9), which is also in agreement with a cool-type outburst.

In the current outburst, during the optical maximum, the temperature reaches approximately $\sim$1.4 x 10^5 K, and the luminosity reaches $\sim$1020 $L_\odot$ compared to the same phase observation taken after 1 orbital cycle of YY Her, which yielded a temperature reaching approximately $\sim$1.3 x 10^5 K, and the luminosity reaches $\sim$830 $L_\odot$. This confirms that the 2021 outburst of YY Her is of the hot type. Furthermore, the emission line ratios of He II to Hβ were enhanced during the outburst, as estimated in this work and by U. Munari et al. (2021). Thus, we conclude that YY Her is showing both cool- and hot-type outbursts as seen in AG Dra. Earlier studies by U. Munari et al. (1997b, 2013) show that there were four

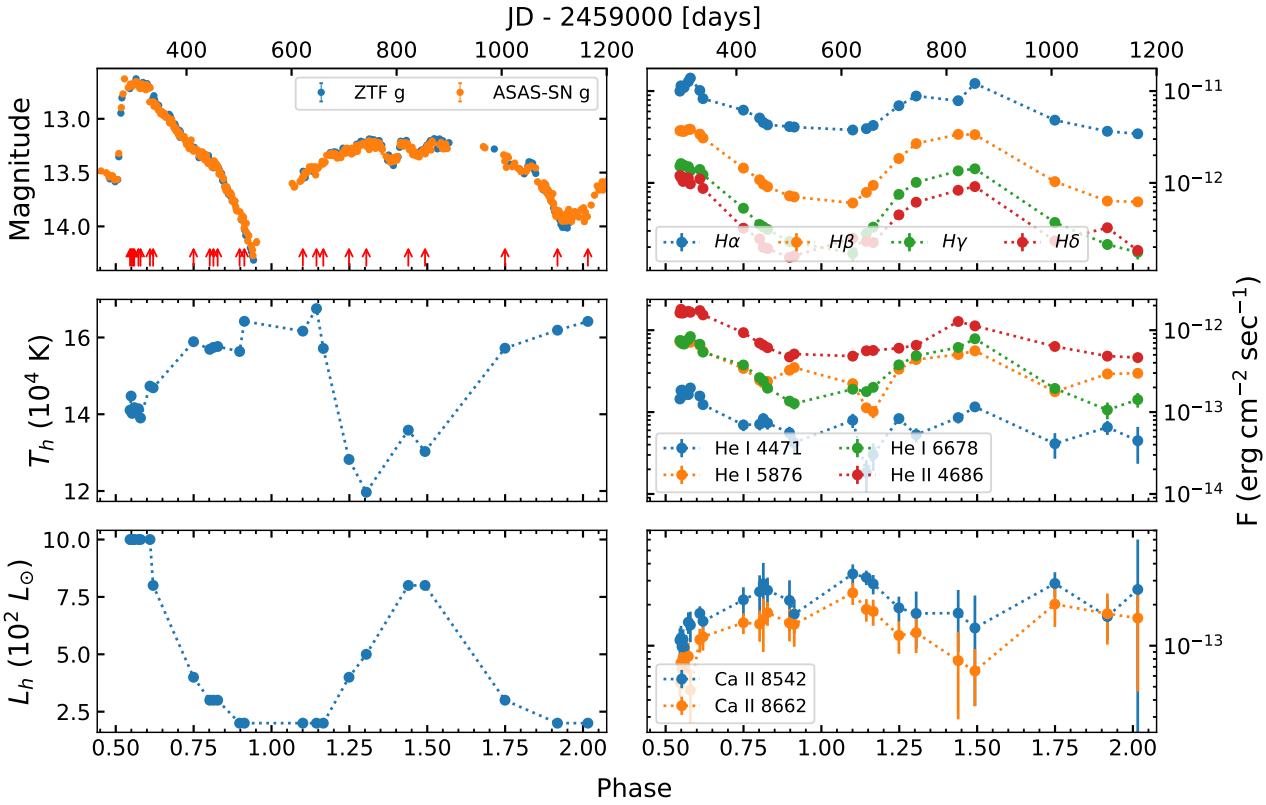

Figure 10. (Top left) ASAS-SN and ZTF g-band light curve with red arrows indicating the epochs of spectroscopic observations. The subsequent plots show the evolution of the temperature and luminosity of the hot component. The second column shows the evolution of line fluxes.

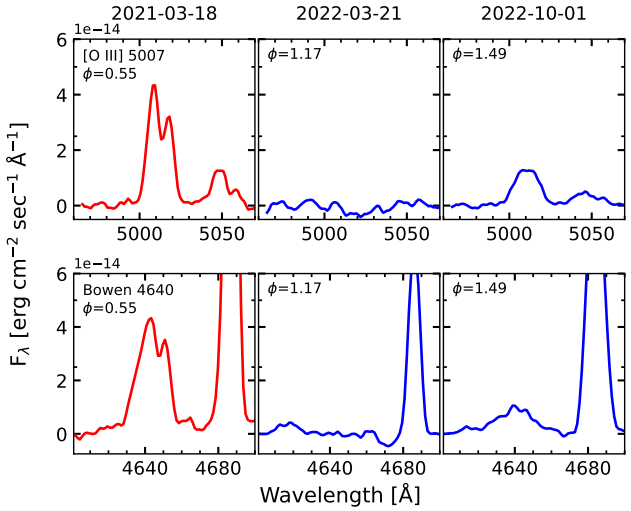

Figure 11. Evolution of O[III] 5007 and Bowen 4640 lines in different phases is plotted (left to right) after subtracting the local continuum. The red color represents the outburst, whereas the blue plots represent the next orbital cycle of YY Her. Interestingly, these lines are only visible at $\phi =$ 0.55 and 1.49, corresponding to secondary minima, and they strengthened considerably during the outburst.

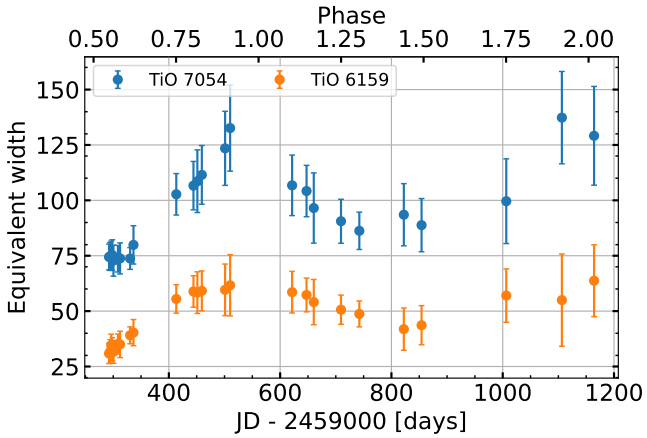

Figure 12. Equivalent widths of TiO bands at 7054 and 6159 Å plotted against time. The upper x-axis shows the orbital phase.

outbursts and brightening events and eight smaller brightening events between 1890 and 2020. The major events have shown an amplitude $\geqslant$2 mag, whereas the minor events are $\sim$1 mag. This is similar to what was reported in AG Dra; the smaller events are hot outbursts, whereas the larger magnitudes could be both cool or hot-type outbursts. Compared to the major outburst reported in 1994, the magnitude of the 2021 outburst is much smaller ($\sim$1 mag), which is consistent with the hot-type outburst.

5. Summary

We have presented a phase-resolved spectroscopic and photometric follow-up of YY Her over 1.5 orbital cycles after its 2021 outburst, combining HFOSC/HCT data with archival light curves.

Our analysis shows that the temperature and luminosity estimation of YY Her is affected by the orbital motion of the system, where the secondary contributes to the modulation of line fluxes, especially low-ionization lines. This causes

Table 2
Hot-component Parameters Derived from Line Fluxes

Date yyyy-mm-dd	JD Since 2400000	Phase	Flux erg cm^{-2} s^{-1}				T_h (10^3 K)	L_h ($L_\odot$)	R_h ($R_\odot$)
			He II 4686 Å	Hβ	He I 4471 Å	He I 5876 Å			
2021-03-18	59292.48	0.55	1.63e-12	3.7e-12	1.45e-13	7.18e-13	141.1	1020.0	0.054
2021-03-20	59294.48	0.55	1.8e-12	3.7e-12	1.83e-13	7.24e-13	144.7	1070.0	0.052
2021-03-22	59296.44	0.55	1.63e-12	3.68e-12	1.86e-13	7.3e-13	140.2	1030.0	0.054
2021-03-24	59298.41	0.56	1.62e-12	3.65e-12	1.6e-13	7.34e-13	141.1	1020.0	0.053
2021-03-26	59300.42	0.56	1.65e-12	3.65e-12	1.72e-13	6.93e-13	141.7	1020.0	0.053
2021-04-03	59308.48	0.57	1.7e-12	3.8e-12	1.64e-13	7.18e-13	141.4	1060.0	0.054
2021-04-07	59312.34	0.58	1.65e-12	3.84e-12	1.97e-13	7.13e-13	139.0	1060.0	0.056
2021-04-25	59330.4	0.61	1.74e-12	3.4e-12	1.57e-13	6.53e-13	147.3	1000.0	0.049
2021-05-01	59336.41	0.62	1.54e-12	3.08e-12	1.23e-13	5.51e-13	146.9	890.0	0.046
2021-07-17	59413.34	0.75	9.3e-13	1.45e-12	7e-14	3.41e-13	158.9	480.0	0.029
2021-08-17	59444.22	0.8	7e-13	1.08e-12	7.1e-14	2.46e-13	156.9	360.0	0.026
2021-08-24	59451.23	0.81	6.6e-13	9.7e-13	8.3e-14	2.28e-13	157.4	340.0	0.025
2021-09-01	59459.26	0.83	6.1e-13	9.1e-13	7.4e-14	2.37e-13	157.7	320.0	0.024
2021-10-13	59501.08	0.9	4.7e-13	7.2e-13	5.6e-14	3.24e-13	156.3	260.0	0.022
2021-10-22	59510.11	0.91	5.1e-13	7e-13	4.2e-14	3.5e-13	164.2	270.0	0.02
2022-02-11	59621.52	1.1	4.8e-13	6e-13	7.9e-14	2.22e-13	161.7	240.0	0.02
2022-03-08	59647.44	1.15	5.6e-13	7.9e-13	1.8e-14	1.13e-13	167.5	270.0	0.019
2022-03-21	59660.45	1.17	5.7e-13	9.4e-13	3e-14	1.01e-13	157.1	290.0	0.023
2022-05-09	59709.38	1.25	6e-13	1.84e-12	8.3e-14	3.34e-13	128.2	460.0	0.043
2022-06-11	59742.3	1.31	6.5e-13	2.68e-12	5.3e-14	4.38e-13	119.7	590.0	0.057
2022-08-30	59822.28	1.44	1.28e-12	3.38e-12	8.6e-14	5.05e-13	135.9	860.0	0.053
2022-10-01	59854.13	1.49	1.13e-12	3.35e-12	1.16e-13	5.6e-13	130.3	830.0	0.056
2023-03-02	60006.39	1.75	6.3e-13	1.03e-12	4.1e-14	1.78e-13	157.2	330.0	0.024
2023-06-10	60106.31	1.92	4.8e-13	6.3e-13	6.5e-14	2.92e-13	161.9	250.0	0.02
2023-08-07	60164.17	2.02	4.6e-13	6.2e-13	4.5e-14	2.98e-13	164.2	240.0	0.019

Note. Dereddened absolute line fluxes of Hβ, He II λ4686, He I λ4471, and He I λ5876 are listed, along with the derived temperature (T_h), luminosity (L_h), and radius (R_h) of the hot component.

overestimation of temperatures during the phases where the cool giant significantly covers the nebular region. Therefore, we consider the estimation of temperature and luminosity in phase 0.5, where the giant does not cover the nebular region and the WD, ensuring reliability.

During the outburst at $\phi = 0.55$, the temperature reached 1.41×10^5 K, and the luminosity reached 1020 $L_\odot$ in the system. During $\phi = 1.49$ after the outburst, the temperature dropped approximately to 1.3×10^5 K, and the luminosity dropped approximately to 830 $L_\odot$ in the system. The post-outburst temperature and luminosity values are notably lower compared to those of the outburst ($\phi = 0.55$). This is in agreement with a hot-type outburst.

During the maxima of 1994–1996 outburst, YY Her showed a drop in temperature and He II 4876 Å/Hβ ratio, which indicates a cool-type outburst characteristic. 2013 and 2021 outbursts show the hot-type outburst characteristics. Hence, we conclude YY Her exhibits both cool and hot-type outbursts similar to AG Dra.

Ca II absorption lines at 8542 and 8662 Å show a periodic variation half that of the orbital period. Since they originate from the cool giant, this is indirect evidence of the ellipsoidal effect. The observed secondary minima of YY Her originate from a combination of sinusoidal variation of the nebular contribution and ellipsoidal modulation of the distorted giant (J. Mikołajewska et al. 2002). The appearance of a magnitude increase during secondary minima after the outburst is attributed to a heated WD at the line of sight ($\phi = 0.5$), suggesting that the hot component may contribute to deeper minima in quiescence. Hence, one cannot rule out the possibility of a contribution from eclipsing to the light curve. It could be possible that both effects may have a role in the observed light curve of the system.

Acknowledgments

The authors thank the staff at IAO, Hanle, and Centre for Research & Education in Science & Technology (CREST), Hosakote, who helped carry out these observations. The IAO and CREST facilities are operated by the Indian Institute of Astrophysics, Bangalore. We also thank all Himalayan Chandra Telescope (HCT) observers for accommodating dedicated time for Target of Opportunity (ToO) observations. We also express our gratitude to the HCT Time Allocation Committee (HTAC) for their support and dedication of time for both ToO and regular observations. This work made use of data from the GROWTH-India Telescope (GIT) set up by the Indian Institute of Astrophysics (IIA) and the Indian Institute of Technology Bombay (IITB) with funding from Indo-US Science and Technology Forum (IUSSTF) and Science and Engineering Research Board, Department of Science and Technology, Government of India (DST-SERB). It is located at IAO. We acknowledge funding by the IITB alumni batch of 1994, which partially supports the operations of the telescope. We thank the anonymous reviewer for comments and suggestions. This study used the open source package Astropy,[8] a Python package for Astronomy (Astropy Collaboration et al. 2018). We acknowledge use of Zwicky Transient Facility data obtained via the NASA/IPAC Infrared Science Archive (IRSA) ZTF Image Service.

[8] http://www.astropy.org

Facilities: HCT, GIT, ASAS-SN, PO:1.2m (ZTF), AAVSO, Gaia.

Software: astropy (Astropy Collaboration et al. 2013, 2018); IRAF (D. Tody 1993); PYRAF (Science Software Branch at STScI 2012).

Appendix
Supplementary Data and Figures

The Appendix contains GIT griz photometry (Table A1), dereddened line fluxes from HCT spectra (Table A2), single- and double-sinusoidal fits to V- and g-band photometry (Figure A1), and supplementary spectra (Figure A2).

Table A1
GIT Photometric Data

JD–2400000	GIT *g*		GIT *i*		GIT *r*		GIT *z*	
	Mag	Error	Mag	Error	Mag	Error	Mag	Error
59618.5	13.510	0.044	12.300	0.023	11.226	0.020	10.640	0.052
59626.5	13.340	0.049	12.108	0.049	…	…	…	…
59631.4	13.424	0.027	12.136	0.045	11.205	0.029	…	…
59631.5	…	…	…	…	…	…	10.592	0.054
59636.4	…	…	…	…	…	…	10.557	0.060
59644.4	13.522	0.064	12.299	0.049	11.268	0.074	10.635	0.059
59649.4	13.452	0.047	12.229	0.040	11.189	0.049	10.617	0.060
59659.4	13.388	0.021	12.090	0.047	11.181	0.039	10.640	0.067
59664.4	13.363	0.042	12.154	0.061	11.164	0.082	10.623	0.068
59675.3	13.293	0.070	12.417	0.088	11.115	0.090	10.597	0.109
59680.3	13.307	0.037	12.194	0.049	…	…	10.658	0.061
59700.3	13.175	0.054	12.136	0.052	…	…	10.542	0.056
59716.2	13.288	0.103	11.984	0.050	11.169	0.084	10.583	0.074
59722.2	13.166	0.059	12.226	0.043	11.072	0.045	10.677	0.093
59722.3	…	…	12.080	0.059	11.186	0.057	10.735	0.092
59722.4	13.285	0.072	…	…	…	…	…	…
59728.2	13.212	0.084	11.891	0.057	11.052	0.033	10.551	0.053
59737.1	…	…	…	…	…	…	10.549	0.079
59737.2	13.218	0.103	11.935	0.043	11.100	0.031	…	…
59738.4	13.305	0.102	11.989	0.050	11.167	0.040	10.624	0.042
59741.4	13.102	0.169	…	…	…	…	…	…
59743.1	13.226	0.090	11.974	0.031	11.104	0.087	10.565	0.124
59749.2	…	…	…	…	11.132	0.030	…	…
59749.3	…	…	…	…	…	…	10.628	0.079
59753.3	…	…	…	…	…	…	10.607	0.051
59763.2	13.194	0.048	11.952	0.046	11.085	0.036	10.598	0.046
59769.4	…	…	11.989	0.074	…	…	10.584	0.136
59785.3	…	…	12.090	0.027	11.258	0.036	10.736	0.049
59820.1	…	…	12.243	0.052	11.279	0.028	10.864	0.108
59820.2	13.145	0.030	…	…	…	…	…	…
59850.2	13.307	0.071	…	…	11.436	0.134	11.102	0.162
59853.2	13.273	0.043	12.175	0.031	11.403	0.033	10.858	0.045
59855.1	13.221	0.061	12.095	0.059	11.331	0.062	10.747	0.075
59858.2	13.215	0.055	12.058	0.056	…	…	10.680	0.097
59873.1	13.222	0.048	…	…	11.256	0.058	…	…
59882.1	13.190	0.026	12.022	0.040	11.246	0.049	10.767	0.082
59894.1	…	…	…	…	…	…	10.661	0.073
60070.2	…	…	…	…	11.306	0.050	…	…
60070.3	13.584	0.030	12.386	0.023	…	…	10.687	0.050
60075.2	13.647	0.032	12.287	0.085	11.311	0.027	…	…
60085.2	13.653	0.030	12.502	0.035	11.513	0.034	10.780	0.067
60090.3	…	…	12.488	0.030	11.385	0.043	10.708	0.071
60090.4	13.673	0.024	…	…	…	…	…	…
60101.2	…	…	12.665	0.037	…	…	…	…
60106.1	13.972	0.039	12.721	0.035	11.486	0.031	…	…
60106.2	…	…	…	…	…	…	10.799	0.042
60111.2	13.966	0.071	12.675	0.040	…	…	…	…
60116.3	13.951	0.031	12.720	0.057	11.652	0.049	10.801	0.085

Note. Photometric data from GIT observations in *g*, *r*, *i*, and *z* filters. Magnitudes and associated errors are provided; Julian Dates are rounded to the nearest 0.1 day.

Table A2
Dereddened Line Flux Measurements

JD–2400000	Hα	Error	Hβ	Error	Hγ	Error	Hδ	Error	He II 4686	Error	He I 4471	Error	He I 5876	Error	He I 6678	Error	Ca II 8542	Error	Ca II 8662	Error
59292.481	998.0	11.0	370.1	4.7	152.1	5.4	119.8	3.3	162.7	3.3	14.50	1.30	71.8	1.6	74.9	1.7	9.9	1.8	5.4	1.2
59294.478	1140.0	11.0	369.6	4.5	162.3	5.8	114.2	3.6	180.1	3.6	18.30	1.80	72.4	1.7	73.6	1.6	10.3	1.6	7.5	1.6
59296.437	1088.0	12.0	367.9	4.3	156.2	4.9	116.0	2.9	162.6	2.9	18.60	1.40	73.0	1.7	68.9	1.7	8.9	1.5	6.8	2.0
59298.411	1093.0	14.0	364.6	4.7	152.4	5.0	103.7	3.1	162.1	3.2	16.00	1.40	73.4	1.9	68.9	1.8	10.0	1.4	8.2	2.9
59300.424	1095.0	14.0	364.5	4.8	155.0	5.3	112.1	3.0	165.5	3.8	17.20	1.50	69.3	1.8	67.7	1.8	8.8	1.5	6.9	1.9
59308.479	1267.0	13.0	380.4	4.4	150.1	5.3	113.3	2.8	170.0	3.8	16.40	1.40	71.8	1.7	77.0	1.7	13.5	1.7	8.4	2.1
59312.338	1384.0	15.0	383.6	5.0	135.6	5.5	97.5	3.2	165.4	4.2	19.70	2.40	71.3	2.2	83.6	2.1	12.8	2.3	4.7	2.0
59330.402	1014.3	9.1	339.6	3.6	139.9	5.9	110.5	2.9	173.5	3.1	15.70	1.50	65.3	1.4	67.4	1.3	15.6	1.4	11.1	2.2
59336.407	827.0	15.0	308.1	5.5	122.9	5.3	87.0	2.5	153.9	3.6	12.30	1.30	55.1	2.0	54.0	2.0	13.7	1.9	11.6	2.4
59413.342	620.0	14.0	145.0	3.3	53.0	2.5	32.1	1.5	93.4	2.7	7.00	1.10	34.1	1.6	37.6	1.9	19.6	3.9	14.7	2.6
59444.219	509.0	15.0	108.2	3.5	35.3	1.9	24.6	1.3	69.7	2.4	7.10	1.10	24.6	1.5	26.3	2.0	22.4	6.5	14.4	3.7
59451.235	455.0	18.0	96.9	3.9	33.2	2.5	19.9	1.6	65.6	2.8	8.30	1.40	22.8	1.9	24.0	2.4	25.6	9.7	15.6	6.6
59459.259	429.0	14.0	90.8	3.3	31.1	2.2	19.3	1.6	61.2	2.7	7.40	1.20	23.7	1.7	19.6	2.1	23.0	4.7	17.5	3.5
59501.079	411.0	16.0	72.3	3.6	23.0	2.6	15.4	1.4	47.1	2.5	5.60	1.00	32.4	2.1	13.6	1.7	19.4	6.9	14.7	3.9
59510.113	406.0	19.0	70.4	3.6	22.6	2.7	16.1	1.9	51.2	3.1	4.20	1.10	35.0	2.3	12.7	1.9	15.3	3.6	14.3	4.5
59621.515	377.0	12.0	60.4	3.0	17.1	2.9	25.0	2.9	48.2	2.4	7.90	1.60	22.2	1.8	19.0	2.2	30.2	4.2	24.4	4.5
59647.436	390.0	11.0	78.8	2.5	28.1	2.4	23.1	1.3	56.0	2.1	1.82	0.77	11.3	1.3	17.8	1.7	28.5	3.1	18.5	3.5
59660.448	422.0	15.0	94.0	4.0	32.9	2.8	22.4	1.5	56.6	2.7	3.00	1.10	10.1	1.7	20.1	2.4	25.6	3.9	17.9	3.9
59709.379	693.0	16.0	184.4	4.1	75.0	2.8	44.9	1.6	60.3	2.2	8.30	1.10	33.4	1.7	37.8	2.0	17.1	3.1	11.9	3.2
59742.300	883.0	15.0	267.8	4.9	101.3	3.0	61.6	2.1	65.4	2.3	5.30	1.00	43.8	1.6	48.8	1.8	15.6	5.2	12.5	3.6
59822.277	785.0	27.0	337.6	9.5	135.1	5.2	83.1	3.1	127.7	4.0	8.60	1.30	50.5	2.5	61.6	3.0	15.7	7.0	7.8	4.9
59854.130	1209.0	34.0	335.1	7.3	142.4	4.4	91.2	2.6	112.9	3.9	11.60	1.10	56.0	2.3	78.6	2.8	12.2	8.3	6.5	2.9
60006.391	482.0	21.0	103.3	5.0	37.1	2.7	23.4	1.7	63.3	3.5	4.10	1.40	17.8	2.3	19.4	3.1	25.8	5.2	20.2	6.4
60106.309	365.0	17.0	63.5	3.4	21.3	2.7	32.5	3.6	48.3	3.0	6.50	1.30	29.2	3.3	10.6	2.5	14.7	4.2	17.2	7.0
60164.172	343.0	24.0	62.2	5.0	17.6	2.9	18.4	2.2	46.3	3.3	4.50	2.10	29.8	2.8	14.2	2.9	23.0	27.0	16.0	11.0

Note. All flux values are in units of $\times 10^{-14}$ erg cm^{-2} s^{-1}. The uncertainties represent propagated errors. Ca II lines are absorption lines, whereas all other lines are in emission.

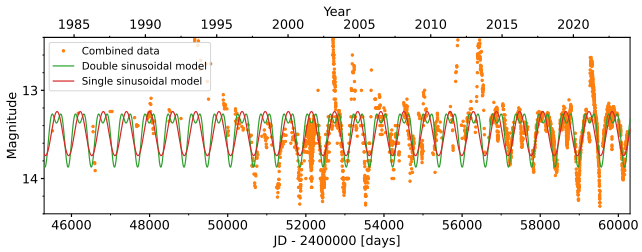

Figure A1. Single and double-sinusoidal models fit on the combined *V*- and *g*-band data. The ephemeris given by Equation (1) is adopted from the double-sinusoidal model.

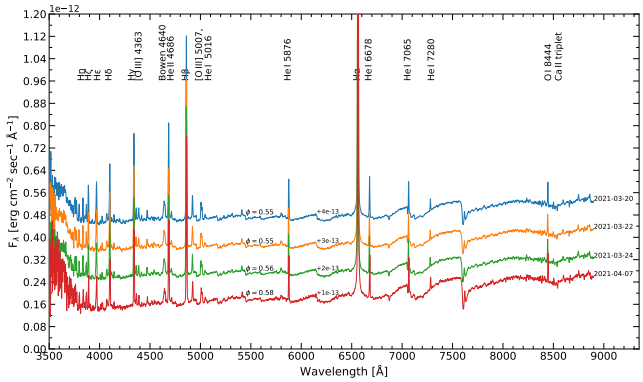

Figure A2. Optical low-resolution spectra of YY Her (not shown in Figure 8), plotted in chronological order. The identified lines are labeled at the top. Observation date and orbital phase (ϕ) are given for each spectrum. Spectra are shifted to the indicated amount for better visibility.

ORCID iDs

L. S. Sonith https://orcid.org/0000-0002-2033-3051
U. S. Kamath https://orcid.org/0000-0003-1729-0190

References

Allard, F., Homeier, D., & Freytag, B. 2012, RSPTA, 370, 2765
Astropy Collaboration, Price-Whelan, A. M., Sipőcz, B. M., et al. 2018, AJ, 156, 123
Astropy Collaboration, Robitaille, T. P., Tollerud, E. J., et al. 2013, A&A, 558, A33
Bailer-Jones, C. A. L., Rybizki, J., Fouesneau, M., Demleitner, M., & Andrae, R. 2021, AJ, 161, 147
Belyakina, T. S. 1970, Ap, 6, 22
Bohme, S. 1939, AN, 268, 71
Brandi, E., Mikołajewska, J., Quiroga, C., et al. 2005, A&A, 440, 239
Bressan, A., Marigo, P., Girardi, L., et al. 2012, MNRAS, 427, 127
Dotter, A. 2016, ApJS, 222, 8
Falcón-Barroso, J., Sánchez-Blázquez, P., Vazdekis, A., et al. 2011, A&A, 532, A95
Fitzpatrick, E. L. 1999, PASP, 111, 63
Formiggini, L., & Leibowitz, E. M. 2006, MNRAS, 372, 1325
Gaia Collaboration, Prusti, T., de Bruijne, J. H. J., et al. 2016, A&A, 595, A1
Gaia Collaboration, Vallenari, A., Brown, A. G. A., et al. 2023, A&A, 674, A1
González-Riestra, R., Viotti, R., Iijima, T., & Greiner, J. 1999, A&A, 347, 478
Green, G. M., Schlafly, E., Zucker, C., Speagle, J. S., & Finkbeiner, D. 2019, ApJ, 887, 93
Hauschildt, P. H., Allard, F., & Baron, E. 1999, ApJ, 512, 377
Henden, A., & Munari, U. 2014, CoSka, 43, 518
Herbig, G. H. 1950, PASP, 62, 211
Hidalgo, S. L., Pietrinferni, A., Cassisi, S., et al. 2018, ApJ, 856, 125
Hric, L., Gális, R., Niarchos, P., & Gazeas, K. 2006, Ap&SS, 304, 307
Hric, L., Petrik, K., Niarchos, P., Velic, Z., & Galis, R. 2001, IBVS, 5046, 1
Husser, T. O., Wende-von Berg, S., Dreizler, S., et al. 2013, A&A, 553, A6
Iijima, T. 1981, Photometric and Spectroscopic Binary Systems (Dordrecht: Springer), 517
Kenyon, S. J. 1986, The Symbiotic Stars (Cambridge: Cambridge Univ. Press)
Kenyon, S. J., & Fernandez-Castro, T. 1987, AJ, 93, 938
Kenyon, S. J., Oliversen, N. A., Mikolajewska, J., et al. 1991, AJ, 101, 637
Kloppenborg, B. K. 2023, Observations from the AAVSO International Database, https://www.aavso.org
Kochanek, C. S., Shappee, B. J., Stanek, K. Z., et al. 2017, PASP, 129, 104502
Kolotilov, E. A., Tatarnikova, A. A., Shugarov, S. Y., & Yudin, B. F. 2002, AstL, 28, 620
Kumar, H., Bhalerao, V., Anupama, G. C., et al. 2022a, AJ, 164, 90
Kumar, H., Bhalerao, V., Anupama, G. C., et al. 2022b, MNRAS, 516, 4517
Lomb, N. R. 1976, Ap&SS, 39, 447
Masci, F. J., Laher, R. R., Rusholme, B., et al. 2019, PASP, 131, 018003
Masetti, N., & Munari, U. 2021, ATel, 14469, 1
Mikołajewska, J. 2012, BaltA, 21, 5
Mikolajewska, J., Acker, A., & Stenholm, B. 1997, A&A, 327, 191
Mikołajewska, J., Kolotilov, E. A., Shugarov, S. Y., Tatarnikova, A. A., & Yudin, B. F. 2003, in ASP Conf. Ser. 303, Symbiotic Stars Probing Stellar Evolution, ed. R. L. M. Corradi, J. Mikolajewska, & T. J. Mahoney (San Francisco, CA: ASP), 151
Mikołajewska, J., Kolotilov, E. A., Shugarov, S. Y., & Yudin, B. F. 2002, A&A, 392, 197
Muerset, U., Nussbaumer, H., Schmid, H. M., & Vogel, M. 1991, A&A, 248, 458
Munari, U. 1989, A&A, 208, 63
Munari, U. 2019, arXiv:1909.01389
Munari, U., Dallaporta, S., Castellani, F., et al. 2013, ATel, 4996, 1
Munari, U., Kolotilov, E. A., Popova, A. A., & Yudin, B. F. 1997a, ARep, 41, 802
Munari, U., Ochner, P., Dallaporta, S., et al. 2021, ATel, 14464, 1
Munari, U., Rejkuba, M., Hazen, M., et al. 1997b, A&A, 323, 113
Munari, U., Siviero, A., Ochner, P., et al. 2009, PASP, 121, 1070
Plaut, L. 1932, AN, 244, 289
Proga, D., Kenyon, S. J., & Raymond, J. C. 1998, ApJ, 501, 339
Proga, D., Kenyon, S. J., Raymond, J. C., & Mikolajewska, J. 1996, ApJ, 471, 930
Rodrigo, C., Solano, E., & Bayo, A. 2012, IVOA Working Draft 15,
Scargle, J. D. 1982, ApJ, 263, 835
Schlafly, E. F., & Finkbeiner, D. P. 2011, ApJ, 737, 103
Science Software Branch at STScI, 2012 PyRAF: Python Alternative for IRAF, Astrophysics Source Code Library, ascl:1207.011
Shappee, B. J., Prieto, J. L., Grupe, D., et al. 2014, ApJ, 788, 48
Skopal, A. 2001, A&A, 366, 157
Skopal, A., Tarasova, T. N., Cariková, Z., et al. 2011, A&A, 536, A27
Skrutskie, M. F., Cutri, R. M., Stiening, R., et al. 2006, AJ, 131, 1163
Sokoloski, J. L., Kenyon, S. J., Espey, B. R., et al. 2006, ApJ, 636, 1002
Sokolovsky, K., Korotkiy, S., Smolyankina, O., et al. 2021, ATel, 14458, 1
Sonith, L. S., & Kamath, U. S. 2023, MNRAS, 526, 6381
Tatarnikova, A. A., Esipov, V. F., Kolotilov, E. A., et al. 2001, AstL, 27, 703
Tatarnikova, A. A., Rejkuba, M., Buson, L. M., et al. 2000, ARep, 44, 190
Tody, D. 1993, in ASP Conf. Ser. 52, Astronomical Data Analysis Software and Systems II, ed. R. J. Hanisch, R. J. V. Brissenden, & J. Barnes (San Francisco, CA: ASP), 173
Vines, J. I., & Jenkins, J. S. 2022, MNRAS, 513, 2719
Wolf, M. 1919, AN, 208, 147
Wright, E. L., Eisenhardt, P. R. M., Mainzer, A. K., et al. 2010, AJ, 140, 1868
ZTF Team 2025, ZTF Lightcurves, IPAC, doi:10.26131/IRSA539